Journal of Rock Mechanics and Geotechnical Engineering 17 (2025) 2893–2903

Contents lists available at ScienceDirect

Journal of Rock Mechanics and Geotechnical Engineering

journal homepage: www.jrmge.cn

Full Length Article

Thermoporoelastic stress perturbations from hydraulic fracturing and thermal depletion in enhanced geothermal systems (EGS) and implications for fault reactivation and seismicity

Mengke An [a, b], Rui Huang [c], Derek Elsworth [b, d], Fengshou Zhang [c, *], Egor Dontsov [e]

[a] Department of Civil and Environmental Engineering, The Hong Kong Polytechnic University, Hung Hom, Kowloon, Hong Kong, China
[b] Department of Energy and Mineral Engineering, EMS Energy Institute and G3 Center, The Pennsylvania State University, University Park, PA, 16802, USA
[c] Department of Geotechnical Engineering, College of Civil Engineering, Tongji University, Shanghai, 200092, China
[d] Department of Geosciences, The Pennsylvania State University, University Park, PA, 16802, USA
[e] ResFrac Corporation, 555 Bryant Street, #185, Palo Alto, CA, 94301, USA

ARTICLE INFO

Article history:
Received 9 March 2024
Received in revised form
12 May 2024
Accepted 28 May 2024
Available online 6 September 2024

Keywords:
Thermoporoelastic stress perturbations
Hot-dry rock
Enhanced geothermal system
Hydraulic fracturing
Thermal depletion
Fault instability

ABSTRACT

Hydraulic fracturing then fluid circulation in enhanced geothermal system (EGS) reservoirs have been shown to induce seismicity remote from the stimulation – potentially generated by the distal projection of thermoporoelastic stresses. We explore this phenomenon by evaluating stress perturbations resulting from stimulation of a single stage of hydraulic fracturing that is followed by thermal depletion of a prismatic zone adjacent to the hydraulic fracture. We use Coulomb failure stress to assess the effect of resulting stress perturbations on instability on adjacent critically-stressed faults. Results show that hydraulic fracturing in a single stage is capable of creating stress perturbations at distances to 1000 m that reach 10^{-5}-10^{-4} MPa. At a closer distance, the magnitude of stress perturbations increases even further. The stress perturbation induced by temperature depletion could also reach 10^{-3}-10^{-2} MPa within 1000 m - much higher than that by hydraulic fracturing. Considering that a critical change in Coulomb failure stress for fault instability is 10^{-2} MPa, a single stage of hydraulic fracturing and thermal drawdown are capable of reactivating critically-stressed faults at distances within 200 m and 1000 m, respectively. These results have important implications for understanding the distribution and magnitudes of stress perturbations driven by thermoporoelastic effects and the associated seismicity during the simulation and early production of EGS reservoirs.

1. Introduction

Geothermal resources in hot-dry rocks have attracted worldwide attention (Zhang et al., 2019a; Aliyu and Archer, 2021; Chen et al., 2022; Wu et al., 2023; Dong et al., 2024) as a low-carbon energy supply. The total worldwide reserves of hot-dry geothermal rocks that are shallower than 10 km approaches 1.3×10^{27} J and could sustain global energy demand at the current usage for ~270 million years (Lu et al., 2018). Consequently, successfully developing this deep hot-dry rock resource is beneficial for both energy supply and for reducing carbon emissions. Well-known projects that pioneered the development of the technology to recover this resource include Fenton Hill and Newberry Volcano Geothermal Reservoirs in the US (Brown and Duchane, 1999; Sonnenthal et al., 2012; Petty et al., 2013; Norbeck et al., 2018), Basel Geothermal Reservoir in Switzerland (Bachmann et al., 2011; Kraft and Deichmann, 2014), Soultz Geothermal Reservoir in France (Calò et al., 2014; Schill et al., 2017), Pohang Geothermal Reservoir in South Korea (Kim et al., 2018a; Kwon et al., 2019) and Gonghe Geothermal Reservoir in China (Lei et al., 2019; Zhang et al., 2021). However, such hot dry rock resources are typically located in ultra-low-permeability metamorphic (e.g. gneiss and basalt) or igneous (e.g. granite and granodiorite) rocks (Baria et al., 1999; Kumari et al., 2018), which makes it difficult to recover the heat. To overcome this limitation, the approach called Enhanced Geothermal System (EGS) has been employed to enhance reservoir permeability and to increase the recovery efficiency of heat (Zimmermann et al., 2010; Olasolo et al., 2016) (Fig. 1).

* Corresponding author.
E-mail address: fengshou.zhang@tongji.edu.cn (F. Zhang).
Peer review under responsibility of Institute of Rock and Soil Mechanics, Chinese Academy of Sciences.

https://doi.org/10.1016/j.jrmge.2024.05.041

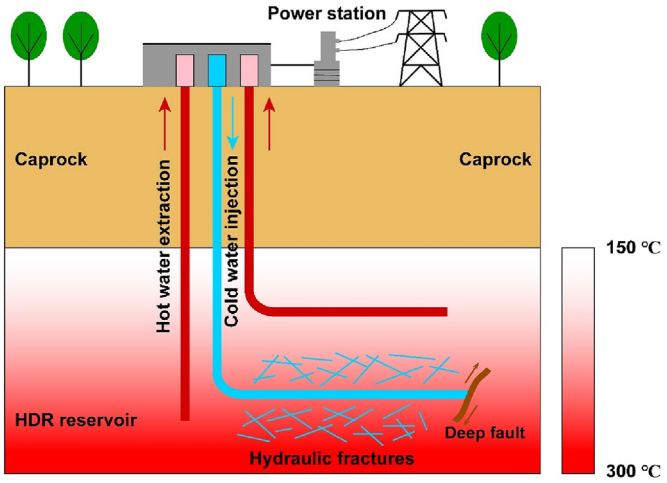

Fig. 1. Schematic showing the layout of an Enhanced Geothermal System (EGS) with injection and production wells. The hot-dry rock (HDR) reservoir is located below the caprock layer. The horizontal well could directly intersect the subsurface deep fault.

However, these EGSs may also cause unwanted environmental consequences. Cold-water injection and hot-water extraction can each reactivate metastable faults and induce earthquakes (Majer et al., 2007; Ellsworth et al., 2019), as observed at Pohang, South Korea, and Gonghe Geothermal Reservoirs, China (Zhang and Hu, 2018; Woo et al., 2019; Zhang et al., 2019b).

The November 2017 Pohang M_w 5.5 earthquake is the largest known induced earthquake at an EGS site (Grigoli et al., 2018; Kim et al., 2018b). It was the most damaging earthquake in the Korean peninsula since the last century (Westaway and Burnside, 2019) that directly injured >100 residents and caused >$300 million in economic losses (Lee et al., 2019a). This earthquake occurred two months after the last fluid injection designed to stimulate the reservoir and this stimulation was implicated in triggering the earthquake (Lee et al., 2019b). The Pohang EGS project involved two injection wells, i.e. PX-1 and PX-2, with both wells reaching a depth of ~4.3 km within the Permian granites. During the drilling of the two vertical wells, significant drilling fluid losses were observed at ~3434 m in well PX-1 and 3816–3840 m in well PX-2, indicating the intersection of the wells with a subsurface permeable fault or fracture (Westaway and Burnside, 2019). A total of five fluid injection tests were performed to stimulate the geothermal reservoir from well PX-1 in December 2016 and August 2017, and from well PX-2 in February, April, and September 2017. In addition to the main earthquake, a cluster of small earthquakes was also observed during fluid injection tests in the two wells (Lee et al., 2019a). By September 2017, the total injection volume in the two wells had reached ~12,000 m^3 with the flowback volume reaching ~7000 m^3 (Hofmann et al., 2019). Currently, it is accepted that the high-pressure fluid injection in well PX-2 reactivated a previously unmapped critically-stressed fault that triggered the earthquake.

China also has significant hot-dry rock resources with the total hot-dry rock resource estimated as ~2.5 × 10^{25} J between depths of 3–10 km, equivalent to ~86 billion tons of coal (Zhang et al., 2020). The Gonghe Geothermal Reservoir in northwestern China is a pilot project for EGS at a depth of ~3705 m with temperature approaching 236 °C (Gao et al., 2018). A number of fracturing-concurrent tests, including fracture diagnostic, acid, slick-water, temporary plugging, and gluing tests were performed on exploration well GR1 (Chen et al., 2021) from August 26, 2019 to August 30, 2019 with injection rates of 0.5–2 m^3/min for a total injected fluid volume of 2.9 × 10^3 m^3. During the five days of hydraulic fracturing, more than 1300 seismic events were detected at depths of 3000–3900 m with earthquake magnitudes (M_L) within the range 0–3 and the largest event reaching magnitude (M_L) ~3 (Chen et al., 2021).

These two examples highlight the importance of understanding the underlying mechanisms of triggering seismicity during the development of the hot-dry rock resource at an EGS site. Tectonic earthquakes are associated with the stability of subsurface faults (Manighetti et al., 2007; Vilarrasa et al., 2016; Huang et al., 2017) with hydraulic fracturing implicated in triggering via the impacts of direct fluid pressurization, thermoporoelastic stress changes and the loading from aseismic slip (Garagash and Germanovich, 2012; Ellsworth, 2013; Rubinstein and Mahani, 2015; Segall and Lu, 2015; Bao and Eaton, 2016; Deng et al., 2016; Elsworth et al., 2016; Eyre et al., 2019). Direct fluid injection may elevate local pore fluid pressure, reduce effective stress, and trigger fault reactivation (Garagash and Germanovich, 2012; Bao and Eaton, 2016; Elsworth et al., 2016). However, this mechanism requires that a direct permeable pathway links the deep fault directly to the injection well (Fig. 1). Loading from fault aseismic slip typically requires that the fault exhibit aseismic slip and creep behavior within the overpressured zone that can transfer stress and induce slip on remote unstable faults and thus trigger seismicity (Eyre et al., 2019). This model is generally applicable to sedimentary reservoirs, such as shale reservoirs (An et al., 2020). Conversely, thermoporoelastic stresses due to fluid injection or extraction and temperature

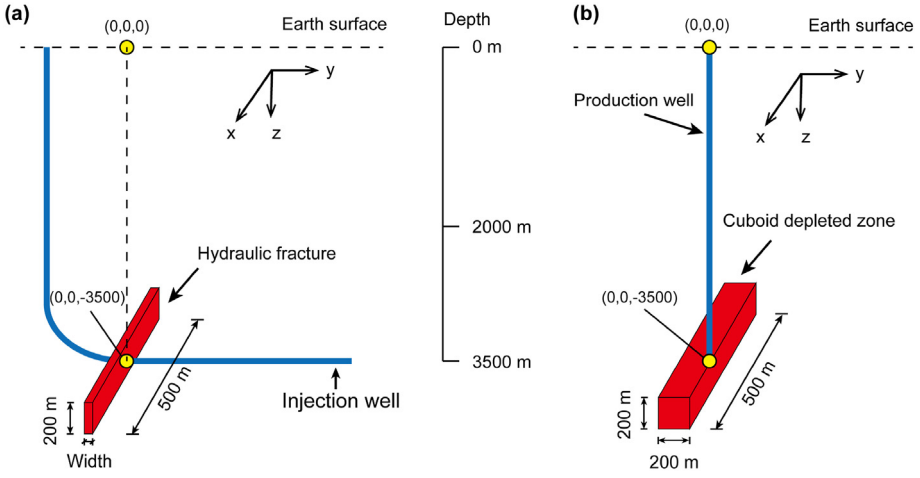

Fig. 2. Schematics of the simplified 3D views of (a) hydraulic fracture and (b) thermal depletion models.

changes may also cause changes in total stress far away from the pressurization zone and with no direct fluid connection – and may also trigger reactivation (Ellsworth, 2013; Rubinstein and Mahani, 2015; Segall and Lu, 2015; Deng et al., 2016; Eyre et al., 2019). Much effort has been devoted to understanding the direct effect of fluid pressure on fault stability – while thermoporoelastic effects are less understood in geothermal reservoirs (Ghassemi and Tao, 2016). Indeed, many current studies ignore the impact of thermoporoelastic stress perturbations from fluid injection and thermal depletion and further do not define the magnitudes of thermoporoelastic stress perturbations - and this remains an important item in determining the fault reactivation potential and understanding the seismic risk (Qiu et al., 2023; Tang et al., 2023).

We address this issue by systematically exploring the magnitude of this thermoporoelastic stress perturbation during EGS reservoir development for a typical system. We use Gonghe EGS in northwestern China as a case study and evaluate the thermoporoelastic stress perturbation that results from hydraulic fracturing and a prismatic depletion zone representing an idealized geometry within a half-space. Note that a uniform temperature change in the prismatic zone is qualitatively equivalent to pressure depletion in the same zone. Quantitatively, however, the result depends on the magnitudes of the pressure and temperature changes as well as material constants. The thermal depletion addressed in this paper represents the process of extracting heat from the reservoir via a heat exchange fluid – the ultimate function of a deep geothermal reservoir. As such, it may be regarded as the opposite process of hydraulic fracturing – as fracturing dilates the fracture from within, while depletion dilates the fracture by contracting the reservoir host. Although, additionally, the hydraulic fracturing also includes the propagation of the fractures. We use Coulomb failure stress as a measure to evaluate the effect of this thermoporoelastic perturbation on the stability of faults in and around the reservoir. For the purpose of this study, the threshold of the change in Coulomb failure stress that is sufficient to trigger instability of critically-stressed faults is taken as 0.01 MPa (Haris, 1998; Stein, 1999). This critical value of 0.01 MPa could be the minimum magnitude to trigger seismicity, although this threshold may be higher than this value in many cases. This study has important implications for understanding the stability of deep faults in hot dry rock reservoirs to ensure the safe recovery of the deep hot-dry rock resource.

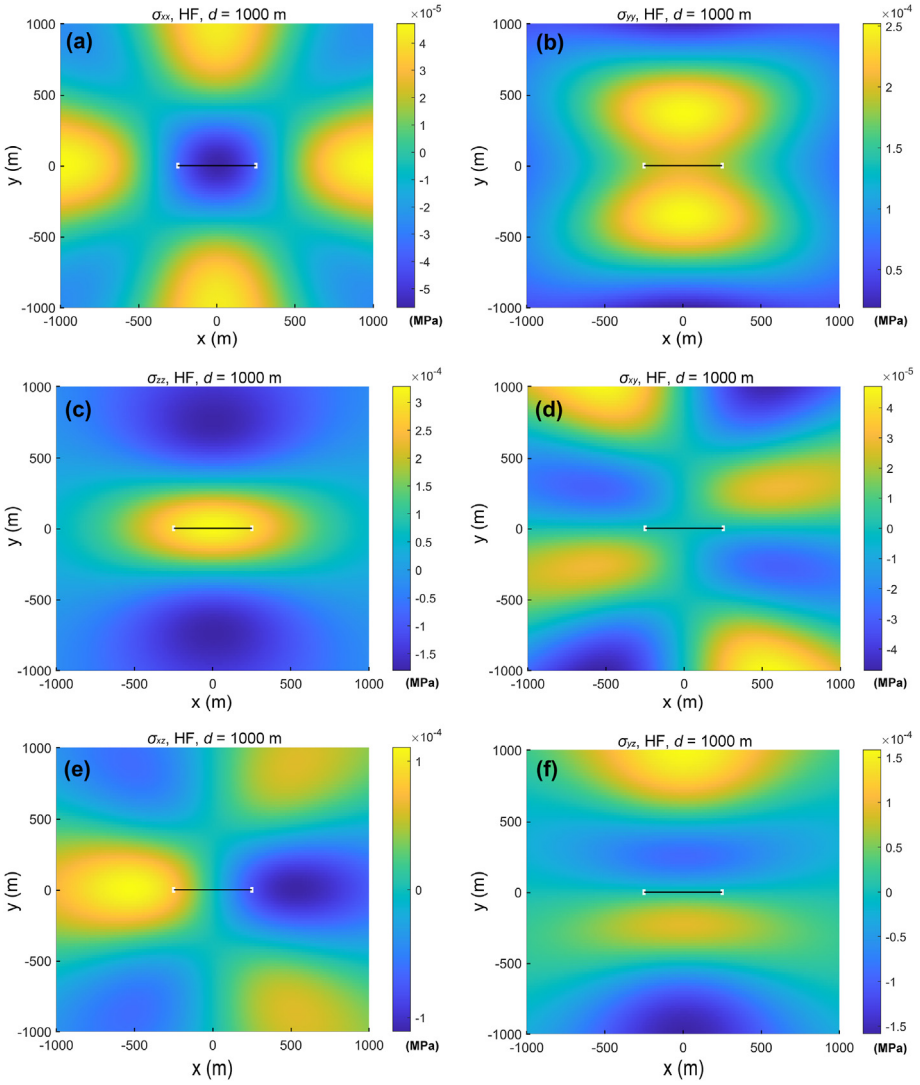

Fig. 3. Contours of poroelastic stress perturbations from a single hydraulic fracture (thin black line) at a distance of 1000 m. The six panels represent the poroelastic stress components (a) σ_{xx}, (b) σ_{yy}, (c) σ_{zz}, (d) σ_{xy}, (e) σ_{xz}, and (f) σ_{yz}, respectively. HF stands for hydraulic fracturing.

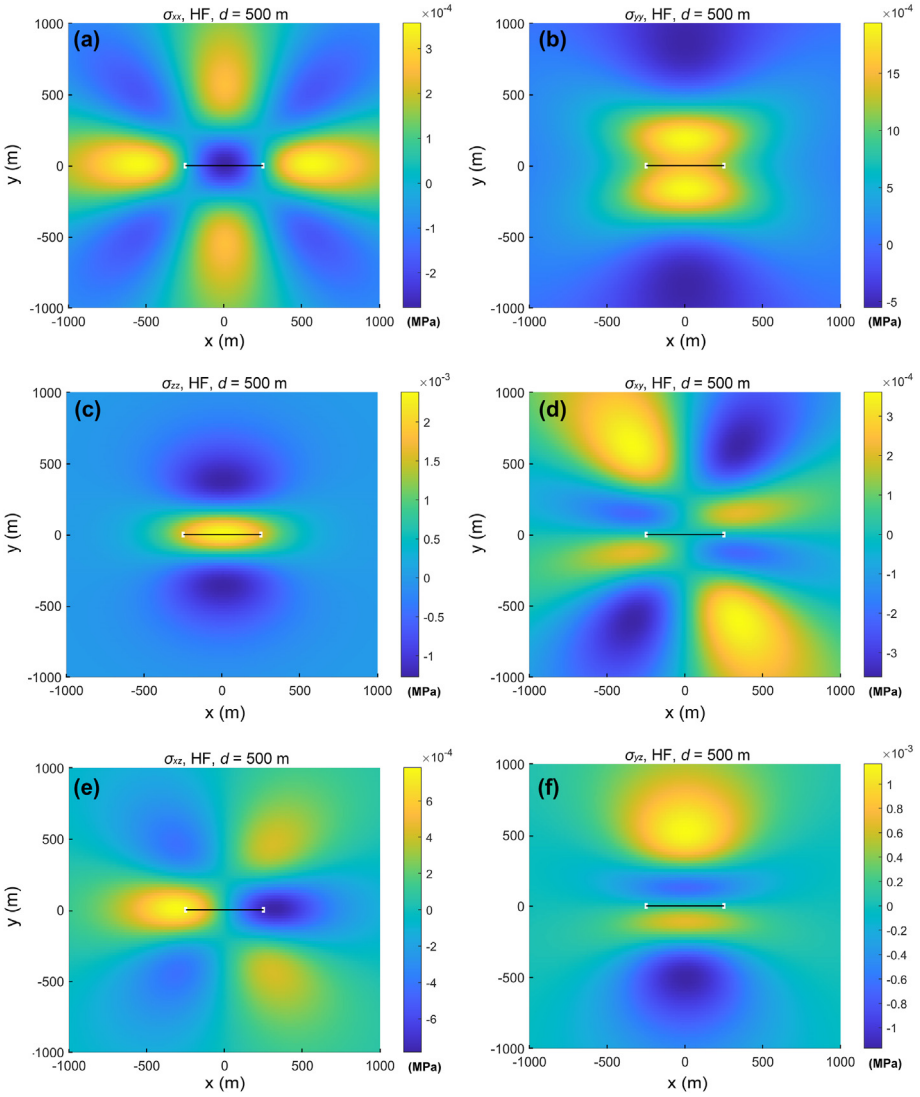

Fig. 4. Contours of poroelastic stress perturbations from a single hydraulic fracture at a distance of 500 m. The six panels represent the poroelastic stress components (a) σ_{xx}, (b) σ_{yy}, (c) σ_{zz}, (d) σ_{xy}, (e) σ_{xz}, and (f) σ_{yz}, respectively.

2. Modeling methods

In this study, we primarily focus on the thermoporoelastic perturbations resulting from a single hydraulic fracturing stage and a prismatic depleted zone around it, to investigate the minimum stress perturbations from an EGS site on deep fault stability. Exploring the minimum stress perturbations aids in defining the minimum requirements for triggering seismicity and thus in guiding hydraulic fracturing operations. Simplified three-dimensional (3D) sketches of a hydraulic fracture and a prismatic depletion zone are shown in Fig. 2. The simplified models are built to honor the typical configuration of the Gonghe geothermal site, in northwestern China and consist of an injection well (horizontal well) (Fig. 2a) and a production well (vertical well) (Fig. 2b). The modeling parameters are consistent with the Gonghe granites with the hydraulic fracturing and thermal depletion zones were all completed at a depth of 3500 m. Hydraulic fracturing and thermal depletion are processes that do not generally operate simultaneously - hydraulic fracturing operates over periods of hours and thermal depletion over days to weeks. Hence, we can explore the resulting stress perturbations independently.

For hydraulic fracturing, a total of 1000 m^3 fluid is assumed to be injected into each fracturing stage. Although multiple fractures may be initiated in each fracturing stage, it is assumed that all fractures in one fracturing stage are combined into a single equivalent symmetric bi-wing fracture with a length of 500 m and a height of 200 m, as shown in Fig. 2a. During the fluid injection, we assume no fluid leak-off and that the fracture width remains uniform. Then, an upper bound for fracture width of 1 cm is obtained given that 1000 m^3 of fluid is injected in a fracture with the dimensions 500 m × 200 m (length × height). We use this upper bound fracture width to estimate the stress perturbations and to evaluate its impacts on fault stability at depth. We set the coordinate system such that the fracture length, width, and height are along the x, y, and z-directions/coordinates, respectively. The origin of the z-axis is set at the Earth's surface and the origins of the x- and y-coordinates are located at the center of the hydraulic fracture. Thus, the coordinates of the fracture center are defined as (0, 0, −3500) (yellow circle in Fig. 2a). Despite of such gross approximation for the fracture, the fracture-induced stress far away from the well is still fairly accurate since the details of fracture geometry smear away from the fracture and the magnitude of the response depends primarily on the total fracture volume.

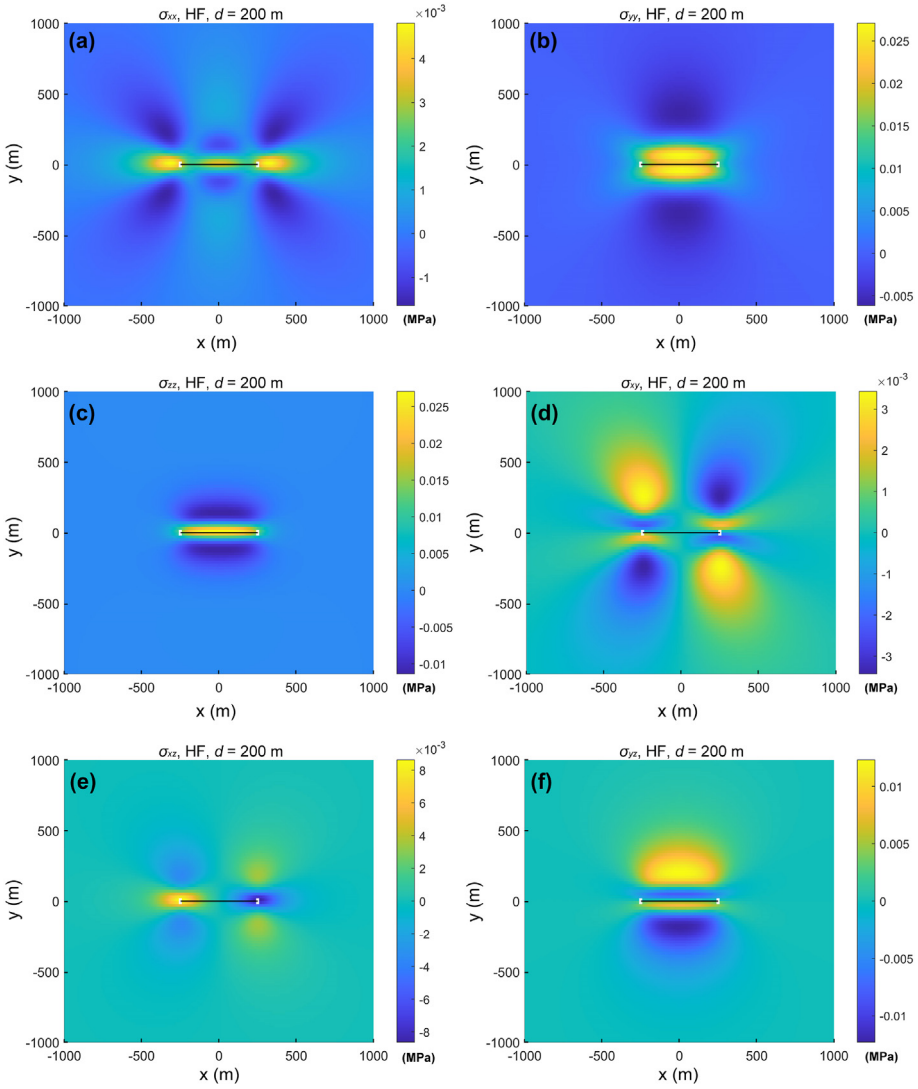

Fig. 5. Contours of poroelastic stress perturbations from a single hydraulic fracture at a distance of 200 m. The six panels represent the poroelastic stress components (a) σ_{xx}, (b) σ_{yy}, (c) σ_{zz}, (d) σ_{xy}, (e) σ_{xz}, and (f) σ_{yz}, respectively.

For thermal depletion, we consider a prismatic depleted zone with the dimensions 500 m × 200 m × 200 m (length × height × width). Note that a uniform thermal drawdown in this region with $\Delta T = \epsilon_m/\alpha_t$ is equivalent to pressure drawdown induced volumetric strain change of $\epsilon_m = \alpha_b \Delta P/K$, where α_t, α_b, and K represent the thermal expansion coefficient, Biot coefficient, and bulk modulus, respectively. The depleted reservoir will shrink as a result of thermal depletion. We assume that the temperature change is ~10 °C after the depletion. By continuing the analogy with pressure depletion, this temperature change is equivalent to ~15 MPa (ΔP = 15 MPa) pore pressure change (considering the thermal expansion coefficient of granite is ~4×10^{-5} K^{-1}) (Plevova et al., 2016). In the modeling, we assume that the pore fluid pressure is uniformly distributed within the hydraulic fracturing or the depletion zone.

The coordinate system for thermal depletion is identical to that for hydraulic fracturing. The length, height, and width of the depleted zone correspond to the *x*-, *y*-, and *z*-coordinates, respectively. The origins of the *x*- and *y*-coordinates are located at the center of the prismatic depleted zone as (0, 0, −3500) (yellow circle in Fig. 2b). For both the hydraulic fracturing and thermal depletion, the elastic modulus (E) of the hot-dry rock reservoir is taken as 50 GPa with a Poisson's ratio (ν) as 0.17. For thermal depletion, the Biot coefficient (α_b) is assumed to be 0.6 (Zhang, 2019). We use the solution of Okada (1992) to determine the displacement around a hydraulic fracture or a prismatic zone in a half-space. The governing equations for the two cases are given in Appendix A. The codes were written by ourselves and all calculations were performed and completed using MATLAB.

3. Results

We calculate the poroelastic stress perturbations from the hydraulic fracture and its prismatic depleted zone following the methods described in Section 2.1. A horizontal area spanning -1000 m $\leq x \leq$ 1000 m and -1000 m $\leq y \leq$ 1000 m is selected to show the results. We plot the poroelastic stress perturbations from the hydraulic fracturing and thermal depletion at a vertical distance of 1000 m and also compare the results with their counterparts at distances of 500 m and 200 m.

3.1. Distributions of poroelastic stress perturbations due to hydraulic fracturing

We first analyze the poroelastic stress perturbations from a hydraulic fracture at a distance of 1000 m. This distance corresponds to the vertical distance between the evaluation plane and

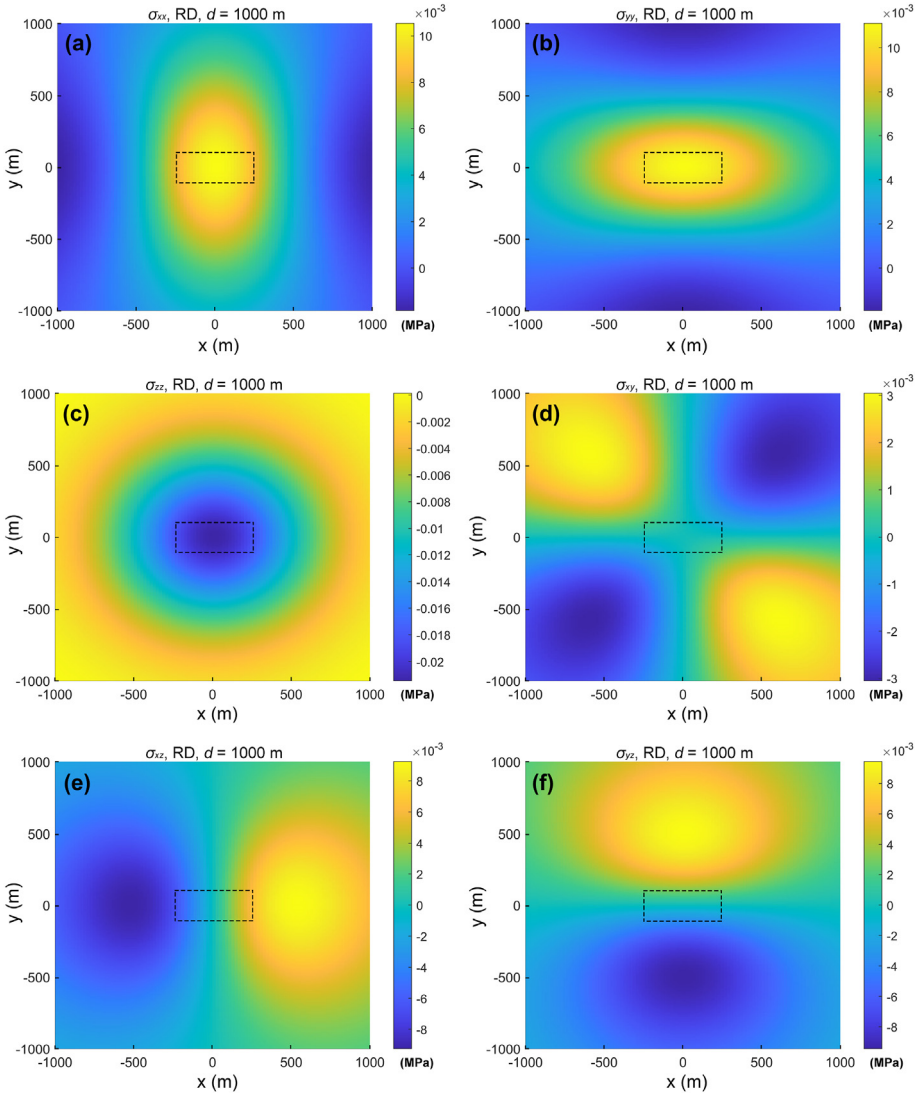

Fig. 6. Contours of poroelastic stress perturbations from a prismatic depleted region (dashed rectangle) at a distance of 1000 m. The six panels represent the poroelastic stress components (a) σ_{xx}, (b) σ_{yy}, (c) σ_{zz}, (d) σ_{xy}, (e) σ_{xz}, and (f) σ_{yz}, respectively. RD stands for reservoir depletion.

the hydraulic fracture center. Contours of poroelastic stress changes from the hydraulic fracture in terms of the six stress components σ_{xx}, σ_{yy}, σ_{zz}, σ_{xy}, σ_{xz}, and σ_{yz} are shown in Fig. 3. The magnitude of the poroelastic stress changes due to hydraulic fracturing at distances of 1000 m are on the order of 10^{-5}-10^{-4} MPa.

Here we employ a notation in which positive poroelastic stress changes correspond to compression. For the σ_{xx} stress component, the fluid injection induces a zone of extension (blue region) around the hydraulic fracture with four compression zones (yellow regions) at the top, bottom, left and right (Fig. 3a). For the σ_{yy} stress component, two large compression zones (yellow regions) are induced at the upper and lower positions of the hydraulic fracture (Fig. 3b). For the σ_{zz} stress component, a single stage of hydraulic fracturing induces a compression zone (yellow region) around the hydraulic fractures, but two extensional zones (blue regions) appear at the top and bottom positions (Fig. 3c). The magnitudes of the σ_{xx} and σ_{xy} stress components are the lowest, near 10^{-5} MPa. Four compression (blue regions) and four extension (yellow regions) zones are developed at the diagonal positions for the σ_{xy} stress component, as shown in Fig. 3d. For the σ_{xz} stress component, the apparent compression (blue region) and extension (yellow region) zones are induced to the left and the right of the hydraulic fracture (Fig. 3d). Conversely, the top and bottom of the evaluation plane show the apparent compression (blue region) and extension (yellow region) zones, respectively (Fig. 3f).

The results at distances of 500 m and 200 m are also evaluated and are presented in Figs. 4 and 5. The magnitudes of poroelastic stress changes are elevated from 10^{-5}-10^{-4} MPa at a distance of 1000 m, to 10^{-4}-10^{-3} MPa at a distance of 500 m, and 10^{-3}-10^{-2} MPa at a distance of 200 m. These results indicate that the magnitudes of poroelastic stresses increase closer to the fracture. Meanwhile, a single stage of hydraulic fracturing induces regions of compression (blue regions) or extension (yellow regions) and these magnitudes also decrease with the increasing distance from the fracture. Compared with Figs. 4 and 5, the area of perturbed stresses resulting from hydraulic fracturing also decreases at a greater distance. The observation that the poroelastic stresses decay rapidly with increasing distance is consistent with the results of Sumy et al. (2014), Lei et al. (2017), and An et al. (2021). However, the magnitudes of poroelastic stresses may be affected by a variety of parameters, including those related to fluid injection, reservoir rock mechanical properties, distances, and geometries.

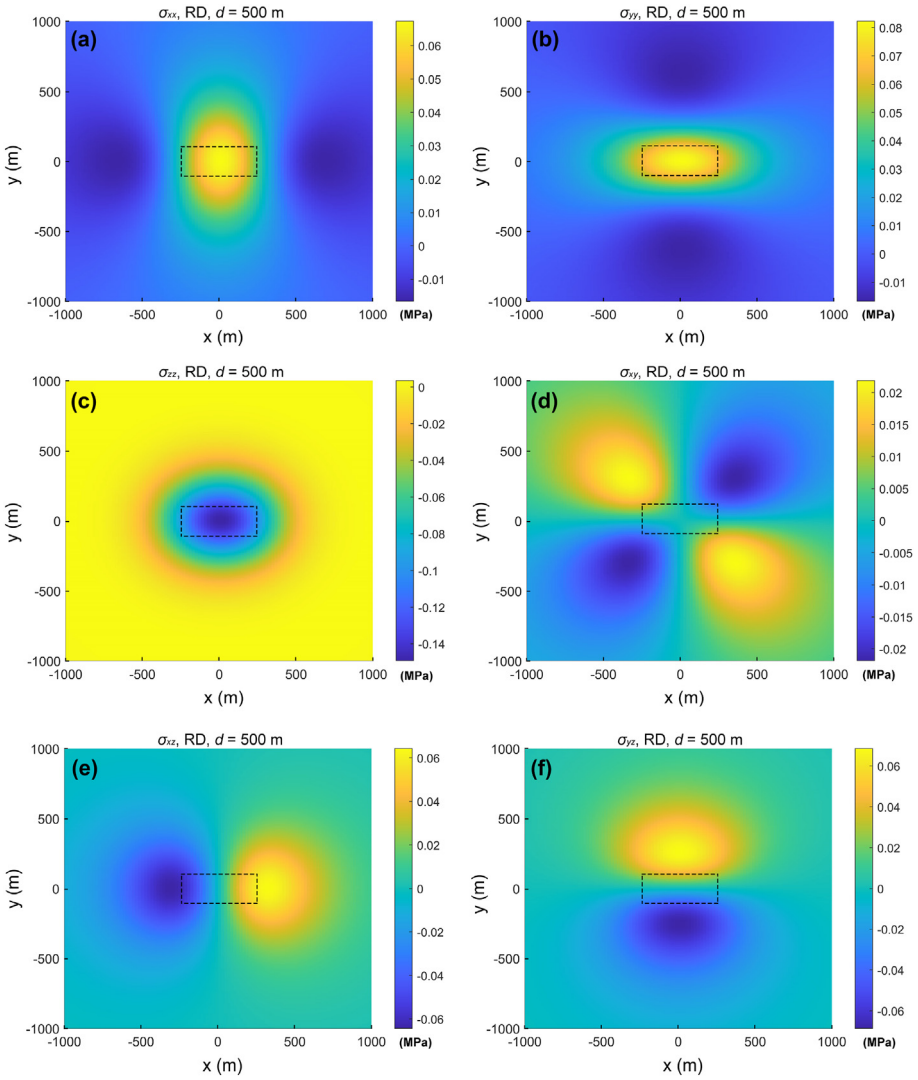

Fig. 7. Contours of poroelastic stress perturbations from a prismatic depleted region at a distance of 500 m. The six panels represent the poroelastic stress components (a) σ_{xx}, (b) σ_{yy}, (c) σ_{zz}, (d) σ_{xy}, (e) σ_{xz}, and (f) σ_{yz}, respectively.

3.2. Distributions of poroelastic stress perturbations due to thermal depletion

We also analyze poroelastic stress perturbations resulting from the quenching of the hydraulically fractured zone – represented as a volumetric contraction of the prismatic depleted zone – specifically at a distance of 1000 m. This is the distance between the evaluation plane and the center of the depletion zone. Contours of the poroelastic stress changes from a prismatic depleted zone on the six stress components σ_{xx}, σ_{yy}, σ_{zz}, σ_{xy}, σ_{xz}, and σ_{yz} are shown in Fig. 6. The magnitude of the poroelastic stress changes due to thermal depletion at 1000 m is within the range 10^{-3}-10^{-2} MPa, much higher than that due the dilating hydraulic fracture.

For the σ_{xx} stress component, the thermal depletion induces an elliptical compression zone (major axis is along the *y*-coordinate) around the prismatic depleted zone and two extension zones on the left and bottom (Fig. 6a). Similarly, the contours of the σ_{yy} stress component also show an elliptical compression zone (major axis is along the *x*-coordinate) around the depleted region, but the two extension zones are located at the top and bottom of the fracture (Fig. 6b). The magnitude of stress change of the σ_{zz} component is the highest (~10^{-2} MPa) among the six stress components and an annular extension zone is formed in the vicinity of $-1000\ \text{m} \le x \le 1000\ \text{m}$ and $-1000\ \text{m} \le y \le 1000\ \text{m}$ (Fig. 6c). Meanwhile, the poroelastic stress change of the σ_{zz} component decreases gradually from the center to the boundary of the evaluation plane. For the σ_{xy} component, the thermal depletion results in the two compression and extension zones at the diagonal positions of the evaluation plane, as shown in Fig. 6d. Contours of the poroelastic stress change of the σ_{xz} and σ_{yz} components both show one compression zone and one extension zone (Fig. 6e and f). However, the extension and compression zones are located on the left and right respectively for the σ_{xz} component, but at the bottom and top respectively for the σ_{yz} component.

The modeling results of thermal depletion at distances of 500 m and 200 m are shown in Figs. 7 and 8. With an increase in the distance between the evaluation plane and the depletion center, the magnitudes of poroelastic stress changes increase from 10^{-3}-10^{-2} MPa at a distance of 1000 m, to 10^{-2}-10^{-1} MPa at a distance of 500 m and 10^{-1}-1 MPa at a distance of 200 m. The results imply that the location greatly influences the poroelastic stress perturbation from the thermal depletion and the magnitude of poroelastic stress change increases closer to the fracture. In addition, the extent of the compression or extension zones also decreases closer

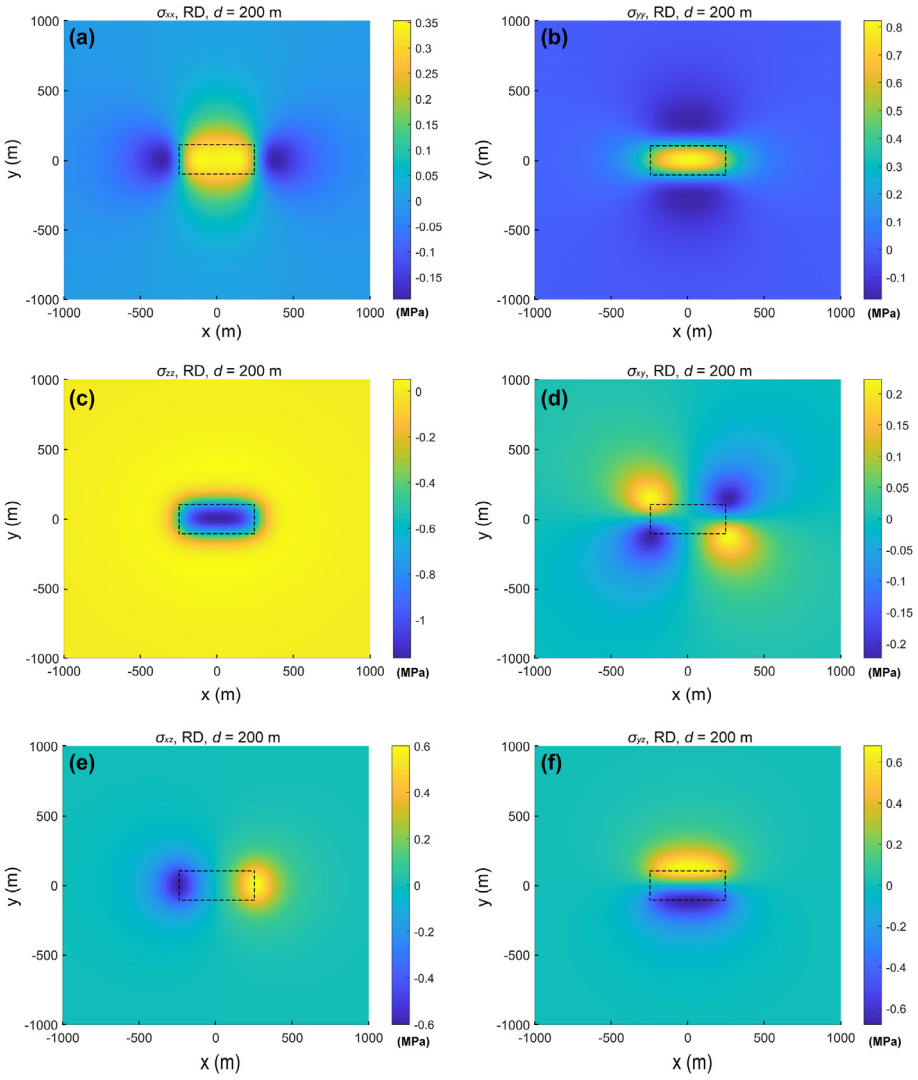

Fig. 8. Contours of poroelastic stress perturbations from a prismatic depleted region at a distance of 200 m. The six panels represent the poroelastic stress components (a) σ_{xx}, (b) σ_{yy}, (c) σ_{zz}, (d) σ_{xy}, (e) σ_{xz}, and (f) σ_{yz}, respectively.

to the fracture (Figs. 6–8), which is consistent with the behavior of stresses caused by hydraulic fracturing, see Section 3.1.

4. Discussion and implications for hot-dry rock fault stability

The stability of faults is commonly evaluated by examining anticipated changes in the magnitude of Coulomb failure stress (*CFS*) (Hill, 2008; Gomberg et al., 2000). For a mature pre-existing fault (ignoring cohesion), fault reactivation occurs when the shear stress (τ) acting on the fault plane is larger than the fault shear strength (τ_f), which can be expressed as

$$\tau \geq \tau_f = \mu_s\left(\sigma_n - P_f\right) = \mu_s\sigma_{neff} \quad (1)$$

where μ_s is the static friction coefficient at the fault plane that is assumed to have the value of 0.7 for Gonghe granite faults/fractures (Zhang et al., 2023; Song et al., 2024), σ_n, P_f, and σ_{neff} represent the normal stress, pore fluid pressure and the effective normal stress acting on the fault plane, respectively. To assess whether a pre-existing fault is becoming more stable or conversely approaching failure, the change in Coulomb failure stress (ΔCFS) is defined from the changes in shear stress and effective normal stress as

$$\Delta CFS = \Delta\tau - \mu_s\left(\Delta\sigma_n - \Delta P_f\right) = \Delta\tau - \mu_s\Delta\sigma_{neff} \quad (2)$$

where $\Delta\sigma_n$, ΔP_f, and $\Delta\sigma_{neff}$ represent the changes of normal stress, pore fluid pressure, and effective normal stress acting on the fault plane, respectively. Positive ΔCFS values indicate that the change of shear stress ($\Delta\tau$) is higher than the change of fault shear strength ($\Delta\tau_f$) and therefore fault reactivation is more likely to occur under this condition. The fault can be reactivated, but it may also exhibit stable sliding or aseismic slip. Many previous studies have indicated that it is sufficient to change the magnitude of Coulomb failure stress (ΔCFS) by only ~10^{-2} MPa for fault reactivation, especially for critically-stressed faults (Harris, 1998; Stein, 1999; Toda and Stein, 2000).

To evaluate the stability of faults present in deep hot-dry rock reservoirs, we assume that the pre-existing granite faults strike along the positive *x*-axis and dip along the positive/negative *y*-axis with dip angles of 15°, 30°, 45°, 60°, and 75°. For hydraulic fracturing, we consider that the hydraulic fracture width is 1 cm and the distance between the evaluation plane and fracture center is

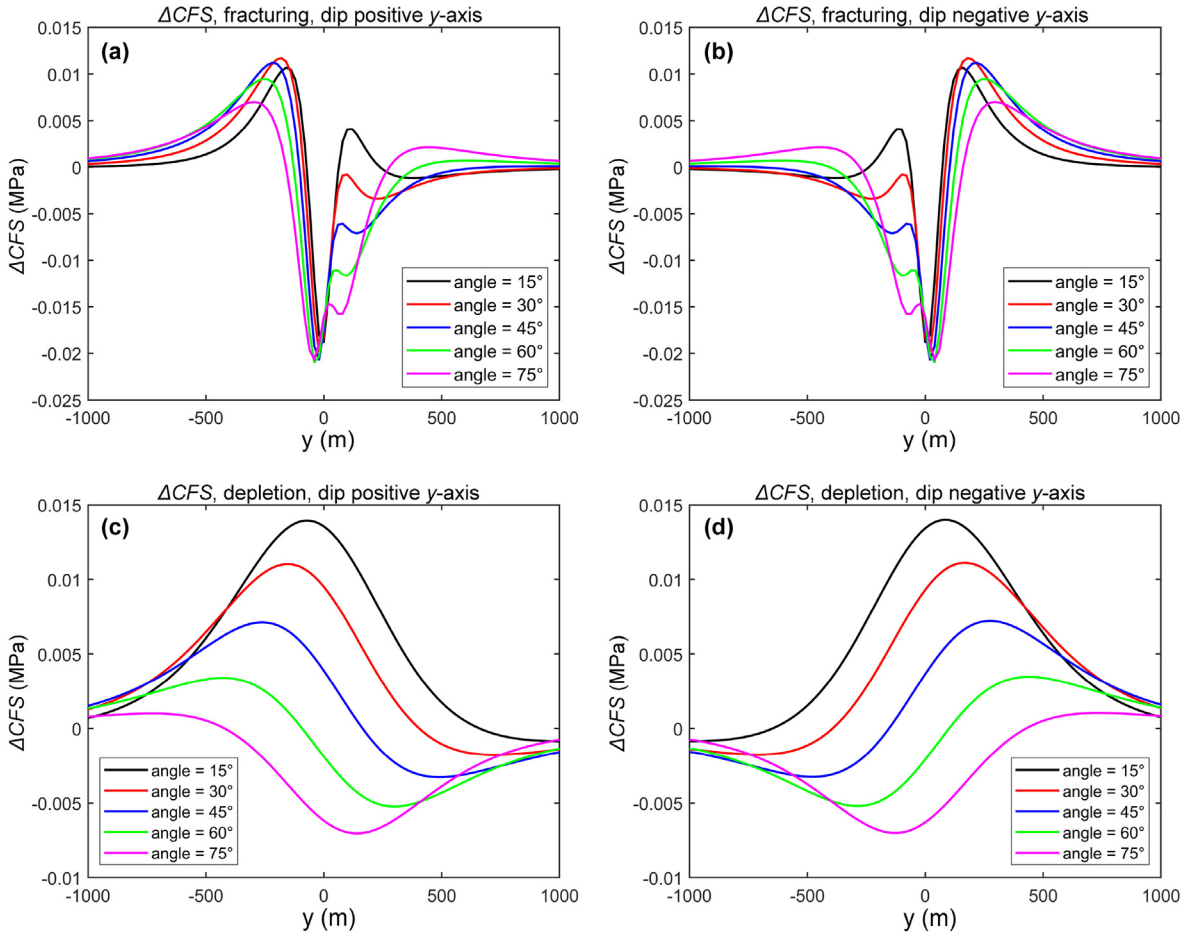

Fig. 9. Δ*CFS* values plotted along the *y*-axis from a single stage of hydraulic fracturing at a distance of 200 m, with the dip directions in (a) positive *y*-axis, and (b) negative *y*-axis. Δ*CFS* values plotted along the *y*-axis from a prismatic depletion zone at a distance of 1000 m, with the dip directions in (a) positive *y*-axis, and (b) negative *y*-axis. The legends show different dip angles.

200 m. The Δ*CFS* values plotted along the *y*-axis from a single stage of hydraulic fracturing for different dip directions and dip angles of 15°, 30°, 45°, 60°, and 75° are shown in Fig. 9a and b. The magnitude of the Δ*CFS* values due to this single-stage hydraulic fracturing approaches 10^{-2} MPa, indicating that a single stage of hydraulic fracturing could reactivate critically-stressed faults within a distance of 200 m. When the distance between the evaluation plane and fracture center exceeds 200 m, such as for 500 m or 1000 m in this study, a single-stage hydraulic fracture may not affect fault stability. However, the above results are only applicable to a single stage of hydraulic fracturing. In field operation, the fluid injection from a single well pad generally involves cyclic fluid injection, and the induced stress perturbations would be much higher than that due to a single stage (Kumar and Ghassemi, 2019). In addition, varying the fault dip directions has a negligible influence on the magnitudes of Δ*CFS* values, while increasing the dip angles from 15° to 75° could not only induce the asymmetry of the results, but also affect the magnitudes of Δ*CFS* values.

For thermal depletion, the temperature change is assumed to be ~10 °C and this corresponds to pore pressure change of ~15 MPa. The distance between the evaluation plane and the prismatic depletion zone is 1000 m. The Δ*CFS* values plotted along the *y*-axis from dip angles of 15°, 30°, 45°, 60°, and 75° are shown in Fig. 9c and d. Here positive and negative dip directions are considered for completeness. The magnitude of Δ*CFS* values from this prismatic depleted zone at a distance of 1000 m also approaches 10^{-2} MPa and thus supports the observation that temperature depletion could also reactivate critically-stressed faults within a distance of 1000 m. As the stress perturbations at distances of 500 m and 200 m are progressively larger than that at a distance of 1000 m (Figs. 7 and 8), the induced Δ*CFS* values at distances of 500 m and 200 m are also larger than that at a distance of 1000 m. Consequently, the seismic potential is higher closer to the depletion zone. However, it should be noted that temperature depletion is gradual and generally changes for months to years and that the Δ*CFS* values due to this prismatic depletion zone will further evolve with time. This may result in delayed seismicity (Gan and Elsworth, 2014a; Gan and Elsworth, 2014b; Rubinstein and Mahani, 2015; Segall and Lu, 2015). In addition, varying the fault dip directions also does not apparently affect the magnitudes of Δ*CFS* values, but would result in the asymmetry of the results and the change in magnitudes of Δ*CFS* values.

5. Conclusions

We calculate stress perturbations resulting from hydraulic fracturing and thermal depletion around an EGS reservoir. We use the Gonghe geothermal reservoir as the case study and Coulomb failure stress to evaluate the impact of stress perturbation on deep fault reactivation. The main conclusions of this study are.

(1) A single stage of hydraulic fracturing can induce stress perturbations on the order of 10^{-5}-10^{-4} MPa at distances of 1000 m. Closer to the fracture, the magnitudes of stress

perturbations increase to 10^{-4}-10^{-3} MPa at a distance of 500 m and then to 10^{-3}-10^{-2} MPa at a distance of 200 m.

(2) Thermal depletion of an idealized prismatic reservoir can induce stress perturbations on the order of 10^{-3}-10^{-2} MPa at a distance of 1000 m - much higher than that due to a single stage of hydraulic fracturing. The stress perturbations from thermal depletion also increase closer to the fracture. The magnitudes of stress perturbations increase to 10^{-2}-10^{-1} MPa at a distance of 500 m and to 10^{-1}-1 MPa at a distance of 200 m.

(3) The Coulomb failure stress is used to evaluate the stability of faults deep within the reservoir. An applied single stage of hydraulic fracturing can influence the stability of deep faults within 200 m of the fracture, while the range of influence from the prismatic thermal depletion is much larger, reaching 1000 m. And in the case of thermal depletion, the magnitude of the effect further grows with time. Besides, the potential seismogenic zone, defined for hydraulic fracturing, also corresponds to the location of the pore pressure diffusion zone, with direct fluid pressurization also affecting fault stability.

(4) Our results have important implications for understanding the stability of faults within and adjacent to hot dry rock reservoirs and the potential for triggering earthquakes on reactivated faults. Both hydraulic fracturing and subsequent thermal depletion can affect the stability of adjacent critically-stressed faults. The stress perturbations would be much higher than these estimates for the case of cyclic hydraulic fracturing and long-term depletion. Thus, it is necessary to evaluate the potential for deep fault instability under these stress perturbations to ensure safe and effective recovery of heat from deep hot-dry rock reservoirs.

CRediT authorship contribution statement

Mengke An: Conceptualization, Data curation, Formal analysis, Writing – original draft. **Rui Huang:** Data curation, Writing – review & editing. **Derek Elsworth:** Data curation, Validation, Writing – review & editing. **Fengshou Zhang:** Data curation, Writing – review & editing. **Egor Dontsov:** Methodology, Software.

Declaration of competing interest

The authors declare that they have no known competing financial interests or personal relationships that could have appeared to influence the work reported in this paper.

Acknowledgments

This research is funded by the National Natural Science Foundation of China (Grant Nos. 42107163 and 42320104003). Derek Elsworth acknowledges support from the G. Albert Shoemaker endowment. We thank the suggestions from Anthony Peirce to calculate the stress perturbations in a half-space.

Appendix A. Supplementary data

Supplementary data to this article can be found online at https://doi.org/10.1016/j.jrmge.2024.05.041.

References

Aliyu, M.D., Archer, R.A., 2021. A thermo-hydro-mechanical model of a hot dry rock geothermal reservoir. Renew. Energy 176, 475–493.
An, M., Zhang, F., Elsworth, D., Xu, Z., Chen, Z., Zhang, L., 2020. Friction of Longmaxi shale gouges and implications for seismicity during hydraulic fracturing. J. Geophys. Res. Solid Earth 125, e2020JB019885.
An, M., Zhang, F., Dontsov, E., Elsworth, D., Zhu, H., Zhao, L., 2021. Stress perturbation caused by multistage hydraulic fracturing: implications for deep fault reactivation. Int. J. Rock Mech. Min. Sci. 141, 104704.
Bachmann, C.E., Wiemer, S., Woessner, J., Hainzl, S., 2011. Statistical analysis of the induced Basel 2006 earthquake sequence: introducing a probability-based monitoring approach for enhanced geothermal systems. Geophys. J. Int. 186, 793–807.
Bao, X., Eaton, D.W., 2016. Fault activation by hydraulic fracturing in western Canada. Science 354 (6318), 1406–1409.
Baria, R., Baumgärtnera, J., Rummel, F., Pine, R.J., Sato, Y., 1999. HDR/HWR reservoirs: concepts, understanding, and creation. Geothermics 28 (4–5), 533–552.
Brown, D.W., Duchane, D.V., 1999. Scientific progress on the Fenton Hill HDR project since 1983. Geothermics 28 (4–5), 591–601.
Calò, M., Dorbath, C., Frogneux, M., 2014. Injection tests at the EGS reservoir of Soultz-sous-Forêts. Seismic response of the GPK4 stimulations. Geothermics 52, 50–58.
Chen, Y., Zhao, Z., Peng, H., 2022. Convective heat transfer of water flow in intersected rock fractures for enhanced geothermal extraction. J. Rock Mech. Geotech. Eng. 14 (1), 108–122.
Chen, Z., Zhao, F., Sun, F., et al., 2021. Hydraulic fracturing-induced seismicity at the hot dry rock site of the Gonghe Basin in China. Acta Geol. Sin.-Engl. 95 (6), 1835–1843.
Deng, K., Liu, Y., Harrington, R.M., 2016. Poroelastic stress triggering of the December 2013 crooked Lake, Alberta, induced seismicity sequence. Geophys. Res. Lett. 43, 8482–8491.
Dong, L., Zhang, Y., Wang, L., Wang, L., Zhang, S., 2024. Temperature dependence of mechanical properties and damage evolution of hot dry rocks under rapid cooling. J. Rock Mech. Geotech. Eng. 16 (2), 645–660.
Elsworth, D., Spiers, C.J., Niemeijer, A.R., 2016. Understanding induced seismicity. Science 354 (6318), 1380–1381.
Ellsworth, W.L., 2013. Injection-induced earthquakes. Science 341 (6142), 1225942.
Ellsworth, W.L., Giardini, D., Townend, J., Ge, S., Shimamoto, T., 2019. Triggering of the Pohang, Korea, earthquake (M_w 5.5) by enhanced geothermal system stimulation. Seismol Res. Lett. 90 (5), 1844–1858.
Eyre, T.S., Eaton, D.W., Garagash, D.I., et al., 2019. The role of aseismic slip in hydraulic fracturing-induced seismicity. Sci. Adv. 5, eaav7172.
Gan, Q., Elsworth, D., 2014a. Analysis of fluid injection-induced fault reactivation and seismic slip in geothermal reservoirs. J. Geophys. Res. Solid Earth 119 (4), 3340–3353.
Gan, Q., Elsworth, D., 2014b. Thermal drawdown and late-stage seismic-slip fault reactivation in enhanced geothermal reservoirs. J. Geophys. Res. Solid Earth 119 (12), 8936–8949.
Gao, J., Zhang, H., Zhang, S., et al., 2018. Three-dimensional magnetotelluric imaging of the geothermal system beneath the Gonghe basin, northeast Tibetan plateau. Geothermics 76, 15–25.
Garagash, D.I., Germanovich, L.N., 2012. Nucleation and arrest of dynamic slip on a pressurized fault. J. Geophys. Res. 117, B10310.
Ghassemi, A., Tao, Q., 2016. Thermo-poroelastic effects on reservoir seismicity and permeability change. Geothermics 63, 210–244.
Gomberg, J., Beeler, N., Blanpied, M., 2000. On rate-state and Coulomb failure models. J. Geophys. Res. Solid Earth 105 (B4), 7857–7871.
Grigoli, F., Cesca, S., Rinaldi, A.P., et al., 2018. The November 2017 M_w 5.5 Pohang earthquake: a possible case of induced seismicity in South Korea. Science 369 (6392), 1003–1006.
Harris, R.A., 1998. Introduction to special section: stress triggers, stress shadows, and implications for seismic hazard. J. Geophys. Res. Solid Earth 103 (B10), 24347–24358.
Hill, D.P., 2008. Dynamic stresses, Coulomb failure, and remote triggering. Bull. Seismol. Soc. Am. 98 (1), 66–92.
Hofmann, H., Zimmermann, G., Farkas, M., et al., 2019. First field application of cyclic soft stimulation at the Pohang Enhanced Geothermal System site in Korea. Geophys. J. Int. 217, 926–949.
Huang, Y., Ellsworth, W.L., Beroza, G.C., 2017. Stress drops of induced and tectonic earthquakes in the central United States are indistinguishable. Sci. Adv. 3 (8), e1700772.
Kim, K.I., Min, K.B., Kim, K.Y., et al., 2018a. Protocol for induced microseismicity in the first enhanced geothermal systems project in Pohang, Korea. Renew. Sustain. Energy Rev. 91, 1182–1191.
Kim, K.H., Ree, J.H., Kim, Y.H., Kim, S., Kang, S.Y., Seo, W., 2018b. Assessing whether the 2017 M_w 5.4 Pohang earthquake in South Korea was an induced event. Science 360 (6392), 1007–1009.
Kraft, T., Deichmann, N., 2014. High-precision relocation and focal mechanism of the injection-induced seismicity at the Basel EGS. Geothermics 52, 59–73.
Kumar, D., Ghassemi, A., 2019. Multistage hydraulic fracturing of EGS wells with application to FORGE. In: Proceedings of the 44th Workshop on Geothermal Reservoir Engineering. Stanford University, Stanford, California, USA.
Kumari, W.G.P., Ranjith, R.G., Perera, M.S.A., et al., 2018. Hydraulic fracturing under high temperature and pressure conditions with micro CT applications: geothermal energy from hot dry rocks. Fuel 230, 138–154.
Kwon, S., Xie, L., Park, S., et al., 2019. Characterization of 4.2-km-deep fractured granodiorite cores from Pohang geothermal reservoir, Korea. Rock Mech. Rock Eng. 52 (3), 771–782.

Lee, K.-K., Ellsworth, W.L., Giardini, D., et al., 2019a. Managing injection-induced seismic risks. Science 364 (6442), 730–732.
Lee, K.-K., Yeo, I.-W., Lee, J.-Y., et al., 2019b. Summary report of the Korean Government Commission on relations between the 2017 Pohang earthquake and EGS project. Geological Society of Korea and Korean Government Commission on the cause of the Pohang earthquake. http://www.gskorea.or.kr/custom/27/data/Summary_Report_on_Pohang_Earthquake_March_20_2019.pdf. (Accessed 20 March 2019).
Lei, X., Huang, D., Su, J., et al., 2017. Fault reactivation and earthquakes with magnitudes of up to M_w 4.7 induced by shale-gas hydraulic fracturing in Sichuan Basin, China. Sci. Rep. 7, 7971.
Lei, Z.H., Zhang, Y.J., Yu, Z.W., et al., 2019. Exploratory research into the enhanced geothermal system power generation project: the Qiabuqia geothermal field, northwest China. Renew. Energy 139, 52–70.
Lu, S.M., 2018. A global review of enhanced geothermal system (EGS). Renew. Sustain. Energy Rev. 81 (2), 2902–2921.
Manighetti, I., Campillo, M., Bouley, S., Cotton, F., 2007. Earthquake scaling, fault segmentation, and structural maturity. Earth Planet Sci. Lett. 253 (3–4), 429–438.
Majer, E.L., Baria, R., Stark, M., et al., 2007. Induced seismicity associated with enhanced geothermal systems. Geothermics 36 (3), 185–222.
Norbeck, J.H., Mcclure, M.W., Horne, R.N., 2018. Field observations at the Fenton Hill enhanced geothermal system test site support mixed-mechanism stimulation. Geothermics 74, 135–149.
Okada, Y., 1992. Internal deformation due to shear and tensile faults in a half-space. Bull. Seismol. Soc. Am. 82 (2), 1018–1040.
Olasolo, P., Juárez, M.C., Morales, M.P., Damico, S., Liarte, I.A., 2016. Enhanced geothermal systems (EGS): a review. Renew. Sustain. Energy Rev. 56, 133–144.
Petty, S., Nordin, Y., Glassley, W., Cladouhos, T.T., Swyer, M., 2013. Improving geothermal project economics with multi-zone stimulation: results from the Newberry Volcano EGS demonstration. In: Proceedings of the Thirty-Eighth Workshop on Geothermal Reservoir Engineering. Stanford University, Stanford, California, USA.
Plevova, E., Vaculikova, L., Kozusnikova, A., Ritz, M., Simha, Martynkova G., 2016. Thermal expansion behaviour of granites. J. Therm. Anal. Calorim. 123, 1555–1561.
Qiu, Y., Ma, T., Liu, J., Peng, N., Xiang, G., Liu, Y., Ranjith, P.G., 2023. Poroelastic response of inclined wellbore geometry in anisotropic dual-medium/media. Int. J. Rock Mech. Min. Sci. 170, 105560.
Rubinstein, J.L., Mahani, A.B., 2015. Myths and facts on wastewater injection, hydraulic fracturing, enhanced oil recovery, and induced seismicity. Seismol Res. Lett. 86 (4), 1060–1067.
Schill, E., Genter, A., Cuenot, N., Kohl, T., 2017. Hydraulic performance history at the Soultz EGS reservoirs from stimulation and long-term circulation tests. Geothermics 70, 110–124.
Segall, P., Lu, S., 2015. Injection-induced seismicity: poroelastic and earthquake nucleation effects. J. Geophys. Res. Solid Earth 120, 5082–5103.
Song, S., Wang, P., Yin, Z., Cheng, Y.P., 2024. Micromechanical modeling of hollow cylinder torsional shear test on sand using discrete element method. J. Rock Mech. Geotech. Eng. https://doi.org/10.1016/j.jrmge.2024.02.010 (in press).
Sonnenthal, E., Spycher, N., Callahan, O., Cladouhos, T., Petty, S., 2012. A thermal-hydrological-chemical model for the enhanced geothermal system demonstration project at Newberry Volcano, Oregon. In: Proceedings of the 37th Workshop on Geothermal Reservoir Engineering. Stanford University, Stanford, California, USA.
Stein, R.S., 1999. The role of stress transfer in earthquake occurrence. Nature 402 (6762), 605–609.
Sumy, D.F., Cochran, E.S., Keranen, K.M., Wei, M., Abers, G.A., 2014. Observations of static Coulomb stress triggering of the November 2011 M5.7 Oklahoma earthquake sequence. J. Geophys. Res. Solid Earth 119 (3), 1904–1923.
Tang, Y., Ma, T., G, J., Mi, G., Ranjith, P.G., 2023. Thermo-poro-elastic analytical model of the heat extraction performance of EGS inlaid with multi-linked fractures. Geoenergy Sci. Eng. 226, 211813.
Toda, S., Stein, R.S., 2000. Did stress triggering cause the large off-fault aftershocks of the 25 March 1998 $M_W = 8.1$ Antarctic plate earthquake? Geophys. Res. Lett. 27 (15), 2301–2304.
Vilarrasa, V., Makhnenko, R., Gheibi, S., 2016. Geomechanical analysis of the influence of CO_2 injection location on fault stability. J. Rock Mech. Geotech. Eng. 8 (6), 805–818.
Westaway, R., Burnside, N.M., 2019. Fault "corrosion" by fluid injection: a potential cause of the November 2017 M_w 5.5 Korean earthquake. Geofluids. https://doi.org/10.1155/2019/1280721.
Woo, J.-U., Kim, M., Sheen, D.-H., et al., 2019. An in-depth seismological analysis revealing a causal link between the 2017 M_w 5.5 Pohang earthquake and EGS project. J. Geophys. Res. Solid Earth 124 (12), 13060–13078.
Wu, H., Liu, Y., Yang, M., Zhang, J., Zhang, B., 2023. Effect of temperature-dependent rock thermal conductivity and specific heat capacity on heat recovery in an enhanced geothermal system. Rock Mech. Bull. (Arch. Am. Art) 2 (2), 100045.
Zhang, C., Hu, S.B., Zhang, S.S., et al., 2020. Radiogenic heat production variations in the Gonghe basin, northeastern Tibetan plateau: implications for the origin of high-temperature geothermal resources. Renew. Energy 148, 284–297.
Zhang, C., Huang, R., Qin, S., et al., 2021. The high-temperature geothermal resources in the Gonghe-Guide area, northeast Tibetan plateau: a comprehensive review. Geothermics 97, 102264.
Zhang, F., Cao, S., An, M., Zhang, C., Elsworth, D., 2023. Friction and stability of granite faults in the Gonghe geothermal reservoir and implications for injection-induced seismicity. Geothermics 112 (3), 102730.
Zhang, J.J., 2019. Applied Petroleum Geomechanics. Gulf Professional Publishing, Houston, TX, USA.
Zhang, L.X., Pang, M.Y., Han, J., Li, Y.Y., Wang, C.B., 2019a. Geothermal power in China: development and performance evaluation. Renew. Sustain. Energy Rev. 116, 109431.
Zhang, W., Qu, Z., Guo, T., Wang, Z., 2019b. Study of the enhanced geothermal system (EGS) heat mining from variably fractured hot dry rock under thermal stress. Renew. Energy 143, 855–871.
Zhang, X.B., Hu, Q.H., 2018. Development of geothermal resources in China: a review. J. Earth Sci. 29 (2), 452–467.
Zimmermann, G., Moeck, I., Bloecher, G., 2010. Cyclic waterfrac stimulation to develop an Enhanced Geothermal System (EGS) — conceptual design and experimental results. Geothermics 39 (1), 59–69.

Mengke An obtained his BSc degree in Civil Engineering from China University of Geosciences (Beijing) in 2015 and his PhD degree in Civil Engineering from Tongji University in 2020. Currently, he is a postdoctoral fellow in Civil and Environmental Engineering at Hong Kong Polytechnic University. His research interests mainly focus on the mechanisms of deep fault stability and induced seismicity during geo-energy extraction and storage, with applications to shale gas exploitation, deep geothermal extraction, and carbon dioxide sequestration/storage. He obtained the CSRME Outstanding Doctoral Dissertation Award in 2021 and the ARMA Rock Mechanics Research Award in 2023.